PROPAGATING WAVE PHENOMENA DETECTED IN OBSERVATIONS AND SIMULATIONS OF THE LOWER SOLAR ATMOSPHERE

D. B. JESS[1], S. SHELYAG[1], M. MATHIOUDAKIS[1], P. H. KEYS[1], D. J. CHRISTIAN[2], AND F. P. KEENAN[1]
[1] Astrophysics Research Centre, School of Mathematics and Physics, Queen's University Belfast, Belfast BT7 1NN, UK; d.jess@qub.ac.uk
[2] Department of Physics and Astronomy, California State University Northridge, Northridge, CA 91330, USA

ABSTRACT

We present high-cadence observations and simulations of the solar photosphere, obtained using the Rapid Oscillations in the Solar Atmosphere imaging system and the MuRAM magnetohydrodynamic (MHD) code, respectively. Each data set demonstrates a wealth of magnetoacoustic oscillatory behavior, visible as periodic intensity fluctuations with periods in the range 110–600 s. Almost no propagating waves with periods less than 140 s and 110 s are detected in the observational and simulated data sets, respectively. High concentrations of power are found in highly magnetized regions, such as magnetic bright points and intergranular lanes. Radiative diagnostics of the photospheric simulations replicate our observational results, confirming that the current breed of MHD simulations are able to accurately represent the lower solar atmosphere. All observed oscillations are generated as a result of naturally occurring magnetoconvective processes, with no specific input driver present. Using contribution functions extracted from our numerical simulations, we estimate minimum G-band and 4170 Å continuum formation heights of 100 km and 25 km, respectively. Detected magnetoacoustic oscillations exhibit a dominant phase delay of $-8°$ between the G-band and 4170 Å continuum observations, suggesting the presence of upwardly propagating waves. More than 73% of MBPs (73% from observations and 96% from simulations) display upwardly propagating wave phenomena, suggesting the abundant nature of oscillatory behavior detected higher in the solar atmosphere may be traced back to magnetoconvective processes occurring in the upper layers of the Sun's convection zone.

Key words: magnetohydrodynamics (MHD) – methods: numerical – Sun: atmosphere – Sun: oscillations – Sun: photosphere

Online-only material: color figures

1. INTRODUCTION

Following the discovery of solar oscillations in the 1960s (Leighton 1960), there has been a multitude of observational evidence brought forward verifying the existence of wave motion in the solar atmosphere (Stein & Leibacher 1974). In more recent years, the role of these oscillations is often closely linked to the search for efficient heating mechanisms of the upper solar atmosphere (see, e.g., Straus et al. 2008; Cauzzi et al. 2009; Taroyan & Erdélyi 2009).

Wave phenomena in the lower solar atmosphere (photosphere and chromosphere) can exist in a variety of different structures, and importantly exhibit various modes of oscillation (Edwin & Roberts 1983). Magnetoacoustic, Alfvén, sausage, and kink modes have recently been observed in a wide range of solar features (De Pontieu et al. 2007; Jess et al. 2007a, 2009; Morton et al. 2011). Importantly, however, is the fact that the majority of these wave phenomena exist in structures which are highly magnetic in nature, such as active regions, pores, and magnetic bright points (MBPs). Indeed, Rimmele et al. (1995) found photospheric oscillations to preferentially exist in intrinsically magnetic intergranular lanes. In the Sun's atmosphere, magnetic field lines clump into tight bundles forming highly structured waveguides, which allow oscillatory motion to be readily channeled along these structures (Shelyag et al. 2010; Fedun et al. 2011a). At any one time it is estimated that up to 2.2% of the entire solar surface is covered by MBPs (Sánchez Almeida et al. 2010), and with their intrinsic magnetic field strengths exceeding 1 kG (Jess et al. 2010a), they may provide the basis of a suitable mechanism for efficient energy transport into the higher layers of the Sun's atmosphere.

Acoustic events occurring in the lower solar atmosphere are often closely examined in an attempt to determine the mechanisms behind, and the energy fluxes associate with, such wave phenomena. Hoekzema et al. (2002) utilized high-resolution ground-based observations to investigate the relation between upwardly propagating acoustic waves and cospatial chromospheric brightenings, while Stein & Nordlund (1991) suggested how acoustic modes may be excited stochastically by non-adiabatic fluctuations in the gas pressure near the solar surface. Highly energetic acoustic waves have been detected by Bello González et al. (2010b) using spectropolarimetric data taken with the IMaX/SUNRISE balloon experiment, with energy fluxes exceeding 7000 W m^{-2} in the low photosphere. Contrarily, Fossum & Carlsson (2005) and Carlsson et al. (2007) examined the presence of acoustic oscillations in the solar chromosphere and concluded that the energy flux of these waves was not sufficiently high to constitute the dominant atmospheric heating mechanism. However, due to telemetry restrictions, the use of data obtained from space-based instrumentation limited their search to oscillations with periods longer than 25 s. This may have resulted in a considerable fraction of energy, at short periods (∼10 s), being overlooked (DeForest 2004; Hasan & van Ballegooijen 2008). Moreover, the contribution functions associated with the filter bandpasses used by Fossum & Carlsson (2005) and Carlsson et al. (2007) are very extended, and must therefore be taken into further consideration (Bello González et al. 2009). Thus, the direct role of acoustic waves in the heating of the solar atmosphere remains uncertain (Kalkofen 2007; Beck et al. 2008; Bello González et al. 2010a). To understand the presence of wave phenomena in the Sun's outer atmosphere, it is imperative to study the photospheric counterpart of these

oscillations, and establish how ubiquitous these fundamental waves are in the lower solar atmosphere. In this paper, we utilize a high cadence multi-wavelength data set to investigate propagating wave phenomena detected in observations and simulations of the lower solar atmosphere.

2. DATA SETS

2.1. Observations

The observational data presented here are part of a sequence obtained during 13:46–14:47 UT on 2009 May 28, with the Dunn Solar Telescope at Sacramento Peak, New Mexico. We employ the Rapid Oscillations in the Solar Atmosphere (ROSA; Jess et al. 2010b) six-camera system to image a $69\rlap{.}''3 \times 69\rlap{.}''1$ region positioned at solar disk center. A spatial sampling of $0\rlap{.}''069$ pixel^{-1} was used for the ROSA cameras to match the telescope's diffraction-limited resolution in the blue continuum to that of the CCD. This results in images obtained at longer wavelengths being slightly oversampled. However, this was deemed desirable to keep the dimensions of the field of view the same for all ROSA cameras.

During the observations, high-order adaptive optics (Rimmele 2004) were used to correct wave-front deformations in real time. The acquired images were further improved through the use of the KISIP speckle reconstruction algorithm (Wöger et al. 2008), utilizing $16 \rightarrow 1$ restorations. Combining consistently excellent atmospheric seeing conditions with speckle image reconstruction, a two-pixel diffraction-limited resolution of ≈ 100 km is achieved for both G-band and 4170 Å blue continuum imaging. For the purposes of this paper, only observations acquired through the photospheric G-band and 4170 Å blue continuum filters will be presented, each with a post-reconstruction cadence of 0.528 s. The G-band and 4170 Å blue continuum filters have central wavelengths of 4305.5 Å and 4170.0 Å, in addition to full width at half-maximums of 9.2 Å and 52.0 Å, respectively. To insure accurate co-alignment in all bandpasses, broadband time series were Fourier co-registered and de-stretched using a 40×40 grid, equating to a $\approx 1\rlap{.}''7$ separation between spatial samples (Jess et al. 2007a, 2008).

2.2. Simulations

We utilize the MuRAM (Vögler et al. 2005) radiative magnetohydrodynamic (MHD) code to investigate whether well-understood magnetoconvection processes can produce comparable phenomena to those detected in our observational time series. This code solves large-eddy radiative three-dimensional MHD equations on a Cartesian grid and employs a fourth-order Runge–Kutta scheme to advance the numerical solution in time. The numerical domain has a physical size of 12×12 Mm^2 in the horizontal direction, 1.4 Mm in the vertical direction, and is resolved by $480 \times 480 \times 100$ grid cells, respectively. Our starting point for the simulations is a well-developed non-magnetic ($B = 0$) snapshot of photospheric convection taken approximately 2000 s (about eight convective turnover timescales) from the initial plane-parallel model. A uniform vertical magnetic field of 200 G was introduced at this stage, and a sequence of 872 snapshots recorded, each separated by a time interval of ~ 2 s. The resulting sequence, which is used for further radiative diagnostics, covers approximately 30 minutes of physical time, corresponding to ~ 4–6 granular lifetimes. Full details of the simulation parameters and domain characteristics can be found in Shelyag et al. (2011b).

The broadband filters used in the optical observations allow us to neglect the effects of line-of-sight velocities and magnetic fields in the radiative diagnostics. Due to a lack of detailed information on absorption line profiles contained within the filter bandpasses, precise computation of the wavelength dependence of emergent intensity within each filter is not necessary. Thus, a simplified and computationally efficient approach of calculating the transmitted filter intensities is used. The methodology, similar to that used by Afram et al. (2011), is based on the ATLAS9 spectral synthesis package of Kurucz (1993). Continuum and line opacity tables were calculated for a realistic solar chemical composition, incorporating a microturbulent velocity, $v_{turb} = 2$ km s^{-1}, and subsequently extracted from the ATLAS9 package using the subset codes XNFDF and DFSYNTHE. This procedure takes into account absorption by diatomic CH molecules. To avoid some of the problems highlighted by Afram et al. (2011), the line opacity wavelength grid between 4290–4400 Å was made denser and centered at the wavelength of the G-band filter transmission maximum. The DELO solver (Rees et al. 1989) was used to numerically integrate the corresponding radiative transport equations for all 480×480 vertical rays of the 872 photospheric snapshots, allowing the computation of the intensity spectra within the 4170 Å and G-band filter bandpasses. Calculated spectra were then convolved with the G-band and 4170 Å filter transmission functions to obtain a true intensity time series, which is directly comparable with our observational data. A more in-depth discussion of the methodology outlined here can be found in Shelyag et al. (2011c).

A natural feature of the numerical simulation is the ability to determine wavelength-dependent contribution functions of emergent radiation for the filter bandpasses which reside within its 1.4 Mm vertical domain. Using previously obtained continuum intensities, as well as continuum and line band absorption coefficients, we determined the corresponding continuum and "band depression" (defined as $(I - I_c)/I_c$, where I and I_c are the emergent and continuum intensities, respectively) contribution functions for our observational G-band (4305.5 Å central wavelength and 9.2 Å bandpass) and 4170 Å continuum (4170.0 Å central wavelength and 52.0 Å bandpass) filters. The band depression contribution functions were calculated from the Rosseland means of the continuum and line absorption coefficients, and based on the definition provided by Gurtovenko et al. (1974) and Magain (1986).

3. ANALYSIS AND DISCUSSION

Overall, the Sun was very quiet on 2009 May 28, with no active regions, pores or large-scale magnetic activity present on disk. However, our ROSA field of view, positioned at the center of the solar disk, contained numerous collections of MBPs, providing an ideal opportunity to examine these kiloGauss structures without the line-of-sight effects associated with off disk-center observations. Figure 1 shows simultaneous G-band and 4170 Å continuum snapshots, revealing a wealth of MBPs, which are particularly visible as intensity enhancements in the G-band filtergram.

3.1. Filter Transmission Profiles

Following speckle image reconstruction, and to assist identification of inherently bright and dim structures, each of the G-band and 4170 Å continuum images were normalized to their mean. To examine the throughput of each filter, an intensity
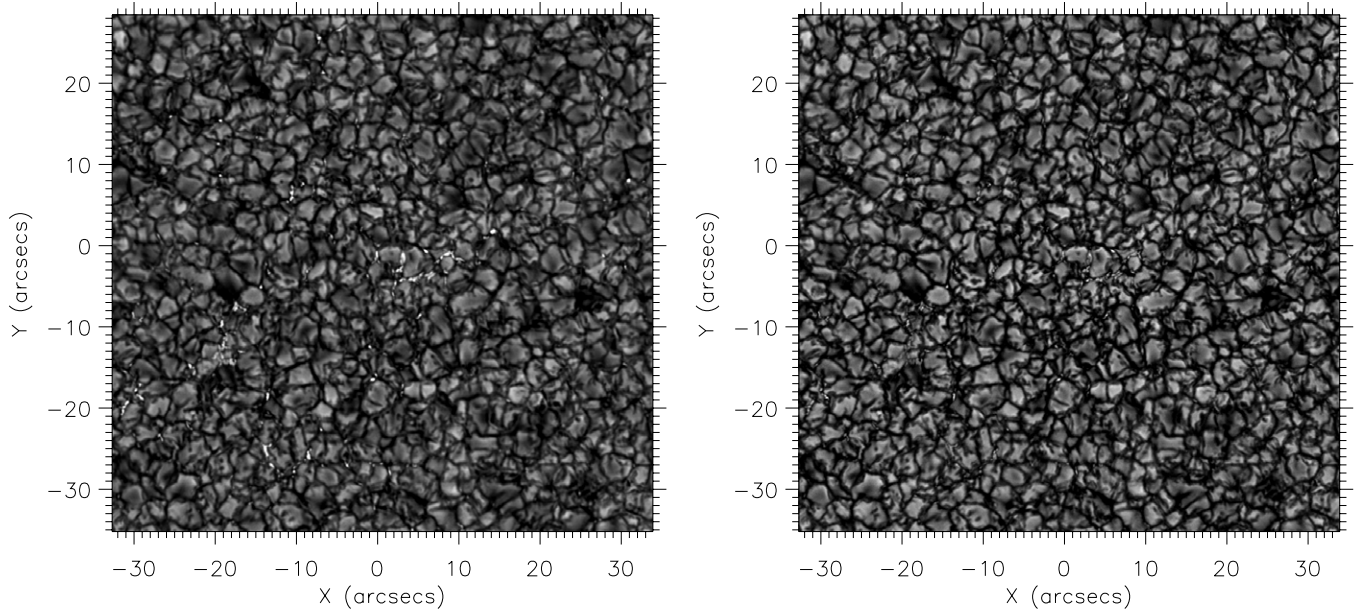
Figure 1. Simultaneous ROSA images acquired through *G*-band (left) and 4170 Å continuum (right) filters at 14:06:21 UT on 2009 May 28. Axes are in heliocentric arcseconds. Note the abundance of MBPs, particularly visible as intensity enhancements in the *G* band.

histogram was created by binning pixel intensities into intervals of 0.05 normalized units. The upper panels of Figure 2 plot histograms of the number of pixels (as a percentage of the total number of pixels) versus normalized intensity, summed over the entire 61 minute duration of the data set (in excess of 7.0×10^9 individual pixels). It is clear from the upper-left panel of Figure 2 that the *G*-band mean is close to its modal value. However, for the 4170 Å continuum observations, the modal value of the images lies below the filter average, suggesting a degree of positive skew in the transmitted intensities. A measurement of the skewness can be determined through the calculation of Fisher and Pearson coefficients of skewness, given by

$$\text{Fisher coefficient} = \frac{\frac{1}{N}\sum_{i=1}^{N}(x_i - \bar{x})^3}{\left(\frac{1}{N}\sum_{i=1}^{N}(x_i - \bar{x})^2\right)^{3/2}} \text{ and} \qquad (1)$$

$$\text{Pearson coefficient} = \frac{3\left(\frac{1}{N}\sum_{i=1}^{N}(x_i) - \tilde{x}\right)}{\left(\frac{1}{N}\sum_{i=1}^{N}(x_i - \bar{x})^2\right)^{1/2}}, \qquad (2)$$

where x_i is the pixel intensity, $\bar{x}$ is the mean, and $\tilde{x}$ is the median, calculated over N independent measurements. While a symmetric distribution will yield a skewness coefficient equal to zero, Fisher and Pearson statistics for the 4170 Å continuum image sequence yield skewness coefficients of 0.39 and 0.36, respectively. A potential weakness of the Fisher coefficient is its sensitivity to anomalous measurements occurring at the extreme ends of the intensity scale. However, consistency with the more robust Pearson coefficient indicates the presence of a well defined, and positively skewed, 4170 Å continuum transmission profile.

Through examination of Figure 1, it is clear that MBPs do not exhibit the same large contrast in 4170 Å continuum images that they do in simultaneous *G*-band snapshots. This can also be verified from the upper-right panel of Figure 2, where the occurrence of 4170 Å continuum intensities falls to zero beyond 1.7 times the mean, compared with *G*-band intensities often exceeding twice the image mean. Interestingly,

an intensity histogram of isolated MBP structures (lower-left panel of Figure 2) reveals that the most commonly occurring MBP intensity is identical ($\approx$1.1 times the image mean) in both bandpasses. However, an extended high-intensity tail is pronounced in the *G*-band MBP histogram, resulting in a high feature contrast for these structures. This elevated contrast is due to its continuum formation level being depressed into deeper (and hotter) layers of the photosphere, where stronger magnetic fields and reduced CH abundances exist. An extended upper intensity range, and subsequently high feature contrast, of *G*-band MBP observations makes them ideal for the detection and tracking of such highly magnetic structures. As a result, we applied the MBP detection and tracking algorithms of Crockett et al. (2009, 2010) and Keys et al. (2011) to create binary maps for each of the *G*-band images. These binary images are used to pinpoint the exact locations within our field of view where MBPs exist, thus allowing their intensity fluctuations to be precisely examined as a function of time.

To investigate whether a shift of MBP intensities to lower values directly contributes to the positive skewness observed in the 4170 Å continuum transmission profile, the MBP binary maps were utilized to mask out locations containing these small-scale structures. The lower-right panel of Figure 2 displays the resulting intensity histogram for non-MBP areas. It is clear that the extended *G*-band high-intensity tail is no longer present, in addition to a substantially reduced profile width near the 4170 Å continuum maximum. Determination of the Fisher and Pearson statistics for the 4170 Å continuum image sequence containing no MBPs yield skewness coefficients of 0.20 and 0.18, respectively. These values are significantly reduced from those derived from the entire field of view, indicating that the lower MBP intensities found in 4170 Å continuum observations directly contributes to the positive skew found in the transmission profile.

3.2. Propagating Wave Phenomena

Following the methodology of Jess et al. (2007a, 2007b), the wavelet analysis routines of Torrence & Compo (1998) were applied to both the *G*-band and 4170 Å continuum time
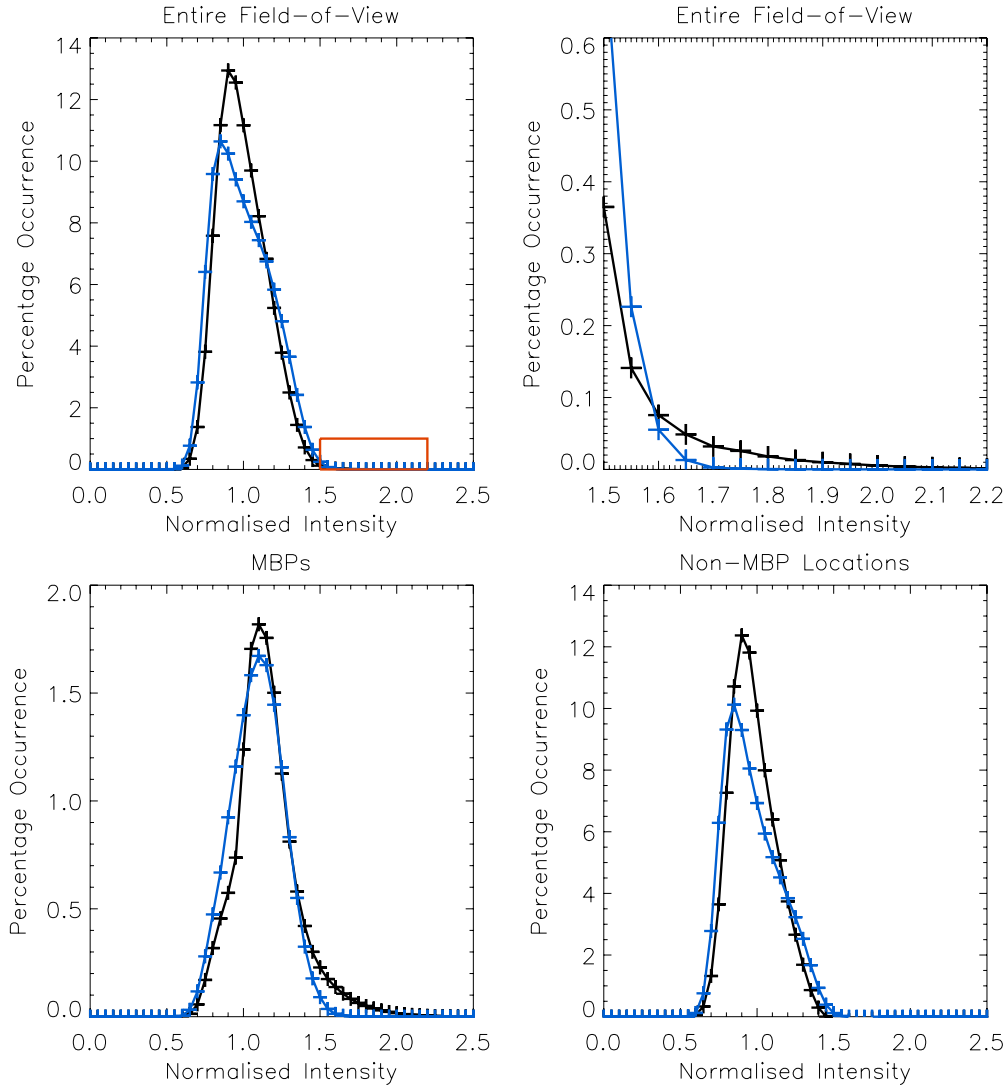
3

Figure 2. Upper left: histograms of the number of pixels, as a percentage of the total number of pixels, vs. their normalized intensity in the *G*-band (black) and 4170 Å continuum (blue) filtergrams, evaluated over the entire 61 minute duration of the data set (7.0×10^9 individual pixels). Upper right: a zoom-in of the intensity occurrences contained within the red box in the left panel. *G*-band intensities display an extended tail, well above the 4170 Å continuum maximum, as a result of the presence of MBPs. Lower left: occurrence of intensities for isolated MBP structures, clearly displaying excess high-intensity measurements for *G*-band observations, also apparent in the upper-right panel. Lower right: intensity histograms for regions of the field of view not containing MBP structures. A narrowing of the 4170 Å continuum profile near its maximum occurrence, caused by the removal of MBP intensities, directly results in the reduction of its positive transmission skewness.
(A color version of this figure is available in the online journal.)

series to search for the presence of oscillatory behavior. Considerable oscillatory power, in both bandpasses, was present throughout the entire field of view, with enhanced concentrations at the locations of MBPs. Due to the image plate scales and camera dimensions being identical for *G*-band and 4170 Å continuum data, no further co-alignment or de-stretching between data sets was required to provide accurate structural alignment. This can be verified visually through the examination of Figure 1. Subsequently, to test the propagation of oscillatory phenomena between the two filters, coherence and phase information between simultaneous *G*-band and 4170 Å continuum pixels were extracted. The resulting data array contained oscillation period (1.056 {Nyquist} → 1830 s), power as a percentage above the background, coherence (0.0 for incoherent waves → 1.0 for coherent oscillations), and phase angle ($-180° \to +180°$) for each of the 7.0×10^9 imaging pixels. Following this nomenclature, a negative phase angle can be interpreted as an oscillation observed in the 4170 Å continuum

leading one also detected in the *G* band. A time-averaged *G*-band image is shown in the left panel of Figure 3, contoured, in the middle panel, with the locations of propagating (i.e., a non-zero phase shift) waves. Approximately 1% of the observational field of view contains propagating waves, with a preferential existence of these oscillations in locations of increased magnetic field strength, such as MBPs (right panel of Figure 3).

To evaluate whether a preferential phase angle existed between *G*-band and 4170 Å continuum oscillations, an occurrence plot, as a function of period and phase angle, was generated for all periodicities which displayed coherence values above 0.85. To differentiate between oscillations occurring in MBP structures from those occurring in the intergranular lanes, the MBP binary maps created above were utilized. By multiplying through each period, power, coherence, and phase angle value by the corresponding pixel binary, an occurrence plot based on where the oscillation was generated can be displayed. The upper panels of Figure 4 show the occurrence distributions for
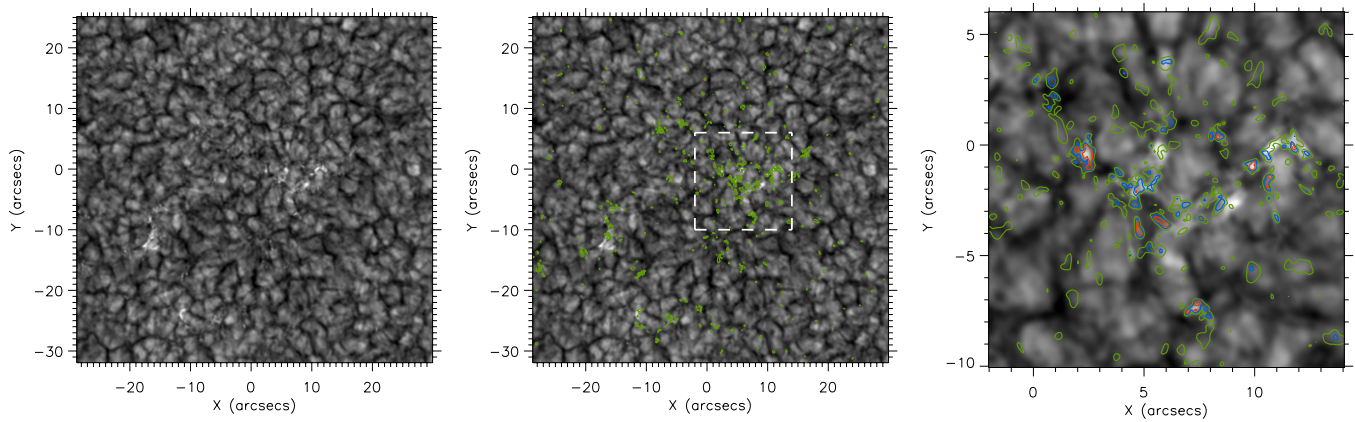
Figure 3. *G*-band intensity image, averaged over the entire 61 minute duration of the time series (left). Green contours (middle and right panels) highlight the locations where waves are observed to propagate (i.e., a non-zero phase shift) between the *G*-band and 4170 Å continuum bandpasses. These contours are generated irrespective of oscillation frequency, and so cannot be used to pinpoint where particular periodicities exist. Dashed white lines outline a sub-field, which is magnified in the right panel. Blue and red contours in the right panel represent propagating wave power which is four and six orders of magnitude, respectively, above the background. A preferential existence of propagating waves is found in locations of increased magnetic field strength, such as MBPs.

(A color version of this figure is available in the online journal.)

oscillations generated in both MBP and non-MBP regions. It is clear that a negative phase shift exists in both panels, with peak occurrences at a phase angle of $-8°$. Positive phase angles do exist, suggesting *G*-band oscillations lead their 4170 Å continuum counterparts in these instances. However, a clear majority of detections (73% for MBP structures and 71% for non-MBP regions) exhibit negative phase shifts, implying a preference for 4170 Å continuum oscillations to lead their *G*-band counterparts. A non-zero phase shift between the detected oscillations suggests that the observed wave phenomena are generated at distinctly different heights in the solar atmosphere and implies the presence of propagating waves. Previous observational and theoretical studies of propagating wave phenomena have indicated their potential for transporting energy away from the solar surface and into higher atmospheric layers (e.g., Carlsson & Stein 1997; Vecchio et al. 2007).

The simulated *G*-band and 4170 Å continuum time series, first interpolated on to a constant-cadence grid, were subjected to the same rigorous wavelet and MBP detection routines as described above. Following the evaluation of period, power, coherence, and phase angle between the simulated data, we are able to create a simulation-specific occurrence plot as a function of period and phase angle, as for the observational data. The middle panels of Figure 4 show the occurrence distributions for oscillations generated in simulated MBP (left) and non-MBP (right) regions. As with the observational time series (upper panels of Figure 4), it is clear that a negative phase shift appears preferential. The peak occurrences are consistent with the observational data, at a phase angle of $-9°$. In the simulated occurrence plot, 96% of MBP structures display a negative phase shift, compared with 95% for non-MBP regions. Also of interest is the number of pixels undergoing oscillations in both the observational and simulated time series. Incorporating both MBP and non-MBP oscillations, a total of 6.06×10^7 observational pixels (0.8% of the 7×10^9 total pixels) are observed to oscillate, compared with 1.62×10^7 simulated pixels (8.1% of the 2×10^8 total pixels). The higher occurrence rate of oscillations in the simulated data is most likely a result of the noise-free time series. Detector dark current, readout noise, and processing abnormalities will reduce the coherence levels of oscillations detected in our observational data set, and thus place them below our strict 0.85 threshold.

Also noticeable in the middle panels of Figure 4 is the reduced spread of phase angles for the simulated occurrence plots. To investigate whether this is a direct consequence of the noise-free time series, noise consistent with the observational data set was added, and the occurrence plots recreated. The acquired data set has a combined photon and read noise of ~1% with respect to the observational count rates. The resulting image signal-to-noise ratio, S/N, can be calculated as S/N $= \mu/\sigma$, where μ is the signal mean and σ is the standard deviation of the noise (Schroeder 2000). A signal mean of ≈5000 counts, combined with a dark frame standard deviation count of ≈19, provides an observational S/N ≈ 260. The addition of 1% noise to the simulated data set did not modify the occurrence plots by a significant margin. However, when the noise level was increased to 5%, the peak occurrence phase angle and oscillation period remained consistent with the noise-free time series, but with a significantly larger spread of phase angles (lower panels of Figure 4). A noise level of 5% provides a simulated S/N ≈ 150, still well above the Rose threshold for feature disambiguation (Rose 1948). Thus, simulated features remain well defined following the addition of 5% noise, yet display a marked increase in the spread of recovered phase angles between the two filter bandpasses. Under these conditions, 80% of MBP structures display a negative phase shift, compared with 79% for non-MBP regions, indicating a closer resemblance to the observational time series. Again, these results imply that, even in the simulated domain, there is a preference for 4170 Å continuum oscillations to lead their *G*-band counterparts.

An important point to raise is how these oscillations are generated. Often, oscillations are produced in simulated time series through the addition of an input driver (e.g., Bogdan et al. 2003; Cally & Goossens 2008; Fedun et al. 2011b). However, in this instance, no specific driver has been added to our time series. This implies that longitudinal oscillations readily arise as a natural consequence of convective motions, and their interaction with the magnetic field in the solar photosphere (see, e.g., Kitiashvili et al. 2011; Shelyag et al. 2011a). Such oscillations have been studied observationally by Goode et al. (1998), who suggested these signatures are the result of events occurring just beneath the photosphere, which subsequently convert into atmospheric longitudinal oscillations. Theoretical approaches
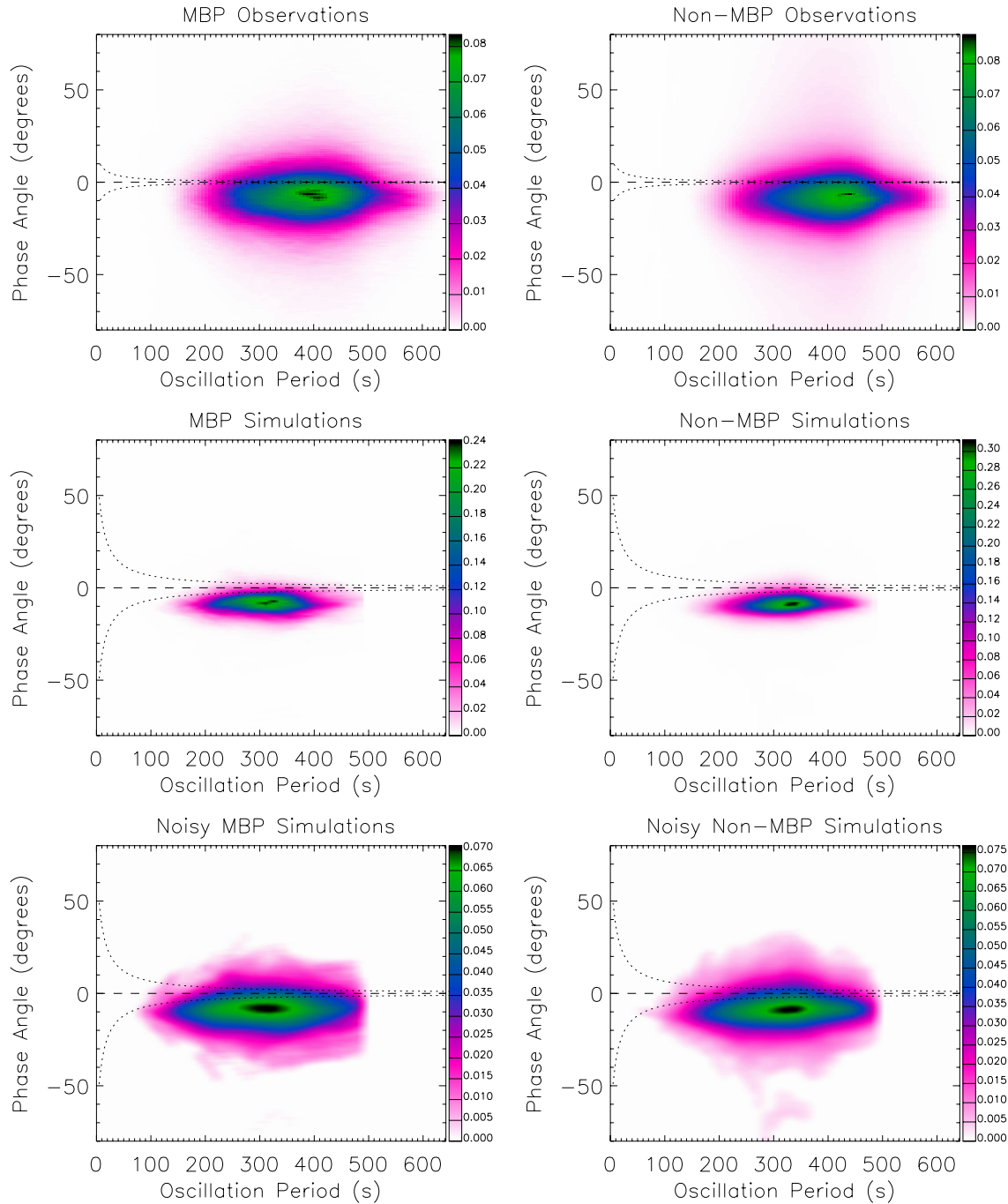
Figure 4. Occurrence of oscillations simultaneously visible in both *G*-band and 4170 Å continuum images, as a function of oscillation period and phase angle for MBP (left) and non-MBP (right) regions. The upper panels represent oscillations occurring in the observational time series, while the middle and lower panels display oscillatory phenomena detected in the noise-free and 5% added noise simulated data sets, respectively. The color scale represents the number of detections as a percentage of the total events with an associated coherence level exceeding 0.85. Consequently, the sum of each panel equals 100%. Dotted lines highlight a region inside which detections become unreliable due to cadence restrictions (0.528 s and 2 s for observational and simulated time series, respectively), while a horizontal dashed line represents a phase angle of 0°. A negative phase shift implies that an oscillation detected in the 4170 Å continuum leads one also detected in the *G* band.

(A color version of this figure is available in the online journal.)

(e.g., Skartlien et al. 2000) have indicated that transient acoustic waves are excited at the top of the convective zone and immediately above convective overshoot regions. Thus, the detection of an abundant array of frequencies over a range of photospheric structures, including MBPs and intergranular lanes, coupled with the rapid development of these oscillatory phenomena, further indicates how the ubiquity of oscillations may be traced back to magnetoconvective processes occurring throughout the solar photosphere.

3.2.1. Determination of formation heights

The contribution functions for our *G*-band and 4170 Å continuum filters are displayed in Figure 5, for both MBP and granular structures, in addition to an average of the entire field of view. Our numerical domain is positioned in such a way that the visible solar surface, roughly defined as the horizontal geometrical layer which is physically close to the optical layer of radiation formation, is located approximately 600 km below
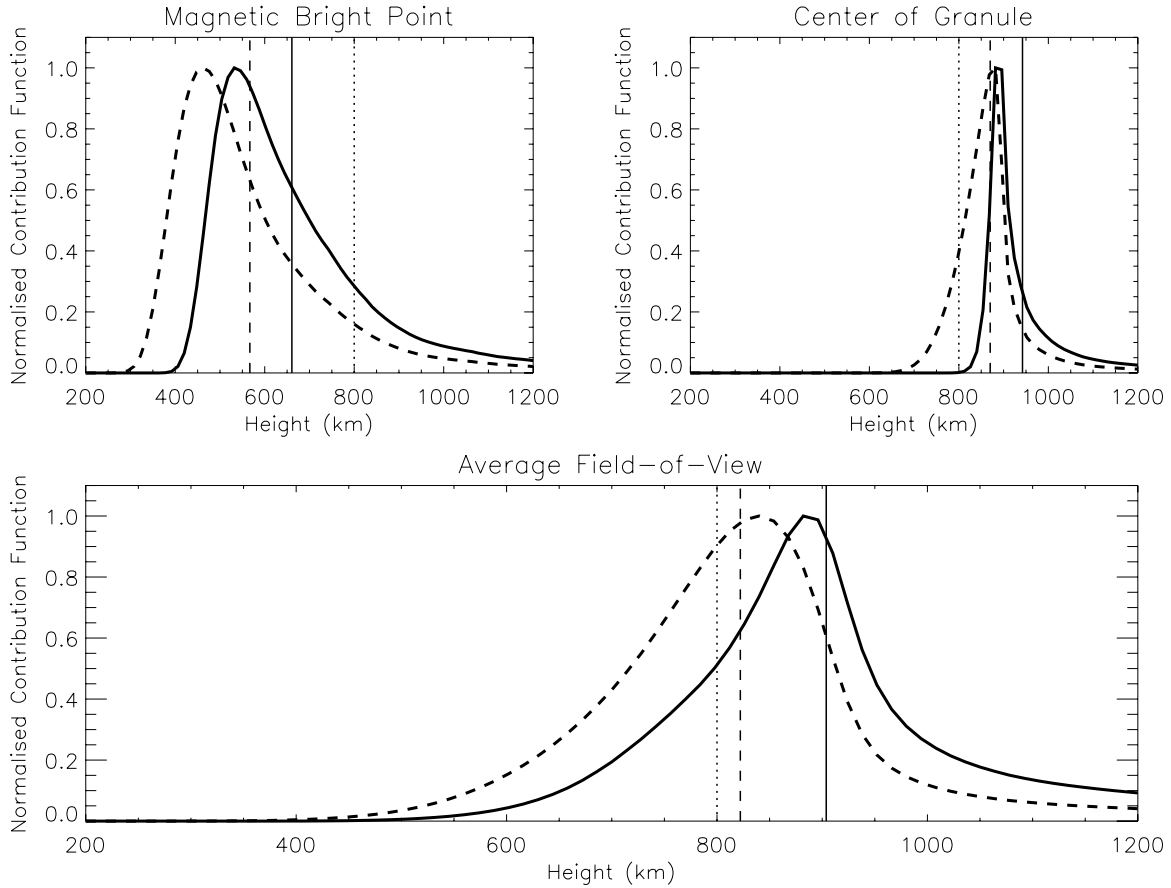
Figure 5. Normalized filter contributions as a function of atmospheric height for *G*-band (solid line) and 4170 Å continuum (dashed line) bandpasses. The upper-left panel displays the contribution functions for a typical MBP, with the upper-right panel presenting contributions arising from the center of a granular cell. The bottom panel represents the contribution functions following a spatial averaging of the entire simulated field of view. A peak separation is clearly visible in the MBP case, while a peak overlap is present for the granular cell. However, due to an extended tail in all *G*-band contribution functions, a measurement of the center-of-gravity separation still yields a height difference in the case of a granular cell, even when the contribution peaks overlap. The atmospheric heights corresponding to the center of gravity of the *G*-band and 4170 Å continuum contribution functions, in addition to the location of the visible solar surface, are represented in each panel by solid, dashed, and dotted vertical lines, respectively. A two-dimensional representation of these methods are shown in Figure 6.

the upper boundary (i.e., at a domain height of 800 km; Shelyag et al. 2011b). Initially, a peak subtraction method was utilized to estimate the height separation between the two filter bandpasses. This process involved establishing the height at which the 4170 Å continuum exhibited its largest contribution, and subtracting this from the simultaneous (and cospatial) peak contribution height for the *G*-band filter. This always resulted in positive distances, ranging from approximately 0 km at the center of granules, to over 200 km in some intergranular lanes and MBPs (upper-right panel of Figure 6). However, from Figure 5, it is clear that the contribution functions for both *G*-band and 4170 Å continuum filters are considerably asymmetric. A prolonged tail, present in the *G*-band contribution functions, suggests that more emphasis should be placed on these extended heights, in order to accurately represent potential height separations. Thus, a center-of-gravity (COG) method was chosen to provide a more robust calculation of the distance between the two filter bandpasses. For each bandpass, the COG was calculated from the corresponding contribution function (CF) using,

$$\mathrm{COG} = \frac{\sum_{i=0}^{z} (\mathrm{CF}_i \times i)}{\sum_{i=0}^{z} \mathrm{CF}_i}, \qquad (3)$$

where *i* represents individual measurements along the simulation's vertical domain, up to a maximum height, *z*, corresponding to 1.4 Mm. The COG measurement for the 4170 Å

continuum bandpass was then subtracted from the simultaneous (and cospatial) COG value derived for the *G*-band filter. Under this regime, all estimated distances were again positive. However, now a minimum height separation of approximately 60 km exists, even for contribution functions acquired at the center of granular cells, where the previous method estimated a 0 km separation. This is a direct result of the inclusion of the extended *G*-band contribution tail seen in Figure 5. The upper-left panel of Figure 6 displays a two-dimensional representation of the estimated atmospheric height separation between *G*-band and 4170 Å continuum filter bandpasses using the COG method. Interestingly, this approach does not provide the same maximum separation distance as found in the peak subtraction method. Using the COG approach, a maximum separation of approximately 170 km was found for some intergranular lanes and MBP structures, compared to a distance of nearly 220 km using the peak separation method. Nevertheless, the two methods provide similar conclusions, whereby the *G* band is formed above the 4170 Å continuum, particularly in regions where strong magnetic field concentrations are expected, such as intergranular lanes and MBPs. In these locations, an average height separation of ≈55 km and ≈83 km is found for the peak subtraction and COG methods, respectively. Furthermore, it is interesting to see how, in the locations of MBPs, the peaks of the *G*-band and 4170 Å continuum contribution functions lie below the layer corresponding to the visible solar surface. This is consistent
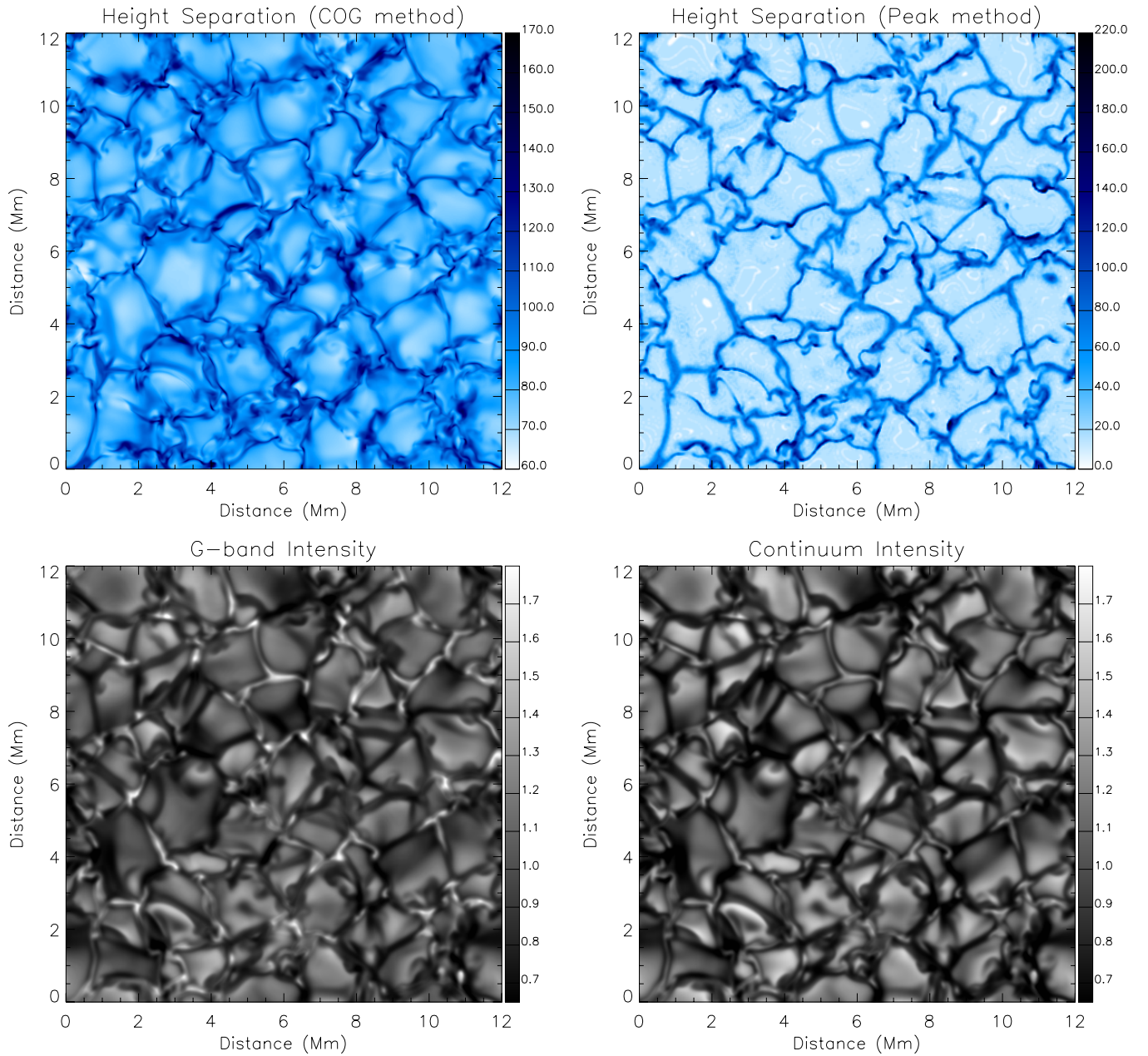
Figure 6. Height separation between *G*-band and 4170 Å continuum bandpasses using the center-of-gravity (upper left) and peak subtraction (upper right) methods. In both upper panels, the color scale represents the separation distance (in km) using each of the methods detailed in Section 3. Simultaneous *G*-band and 4170 Å continuum intensity images, normalized to their mean, are shown for reference in the lower-left and right panels, respectively. All axes are distances along the solar surface, where 1 Mm = 1000 km ≃ 1″.38.

(A color version of this figure is available in the online journal.)

with the detailed models of Spruit (1976), Schüssler et al. (2003), and Shelyag et al. (2004, 2010), who describe how the creation of MBPs is a result of the tenuous interplay between hot photospheric plasma and evacuated magnetic flux tubes.

The formation height for each filter bandpass can also be estimated by applying these techniques to the averaged field-of-view contribution functions. Using the peak subtraction method, a formation height of ∼85 km and ∼40 km above the visible surface (located at ∼800 km in Figure 5) is found for *G*-band and 4170 Å continuum filters, respectively. When the COG method is utilized, the formation heights of *G*-band and 4170 Å continuum bandpasses become modified slightly to ∼100 km and ∼25 km, respectively. It must be noted that these are lower

limits of the height of formation. Molecular and atomic line absorption profiles, which exist in the filter's spectral bandpasses, will contribute to the overall radiation absorption, thus shifting the total (continuum + line) contribution functions. As a result, this will push radiation formation ranges upward toward the cooler regions of the solar photosphere. Consequently, while the *G* band will continue to be formed above the 4170 Å continuum, the exact formation heights will be based on the lower limits established above. This has important consequences for the phase angles determined between simultaneous *G*-band and 4170 Å continuum oscillations. Since the height separation between the 4170 Å continuum and the *G* band is always positive, a negative phase shift can be attributed to an upwardly propagating
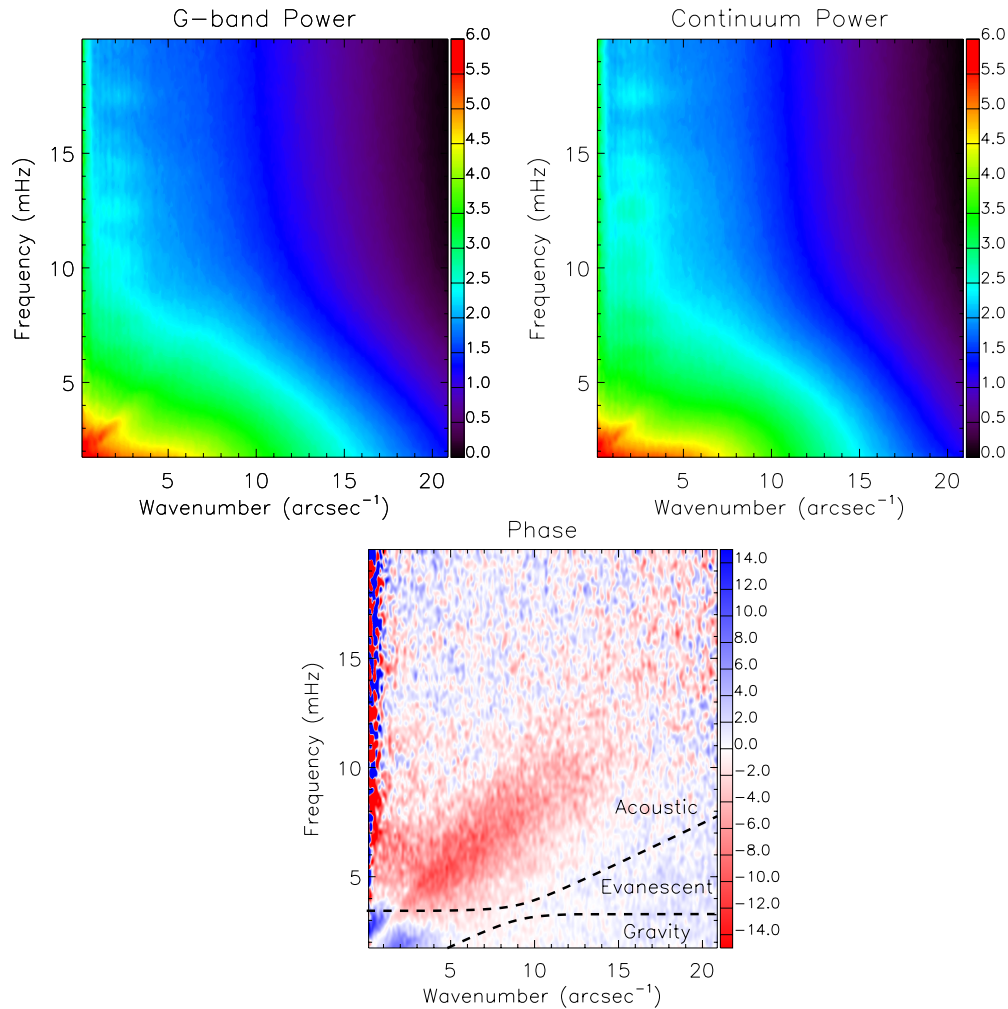
Figure 7. Power spectra of the *G*-band (upper left) and 4170 Å continuum (upper right) observations as a function of frequency and spatial wavenumber. The color scale represents the power (in orders of magnitude) above the quiescent background. The lower panel shows the phase delay between the *G*-band and 4170 Å continuum oscillations as a function of frequency and spatial wavenumber. The color scale is in degrees, where positive and negative values indicate that the *G* band leads, and trails, the 4170 Å continuum, respectively. Limiting curves for acoustic- and gravity-wave regimes are displayed as dashed lines, with an evanescent region sandwiched between the acoustic and gravity regimes. A similar figure, only for the simulated time series, is shown in Figure 8.

(A color version of this figure is available in the online journal.)

wave, such as those studied numerically by Wedemeyer et al. (2003, 2004). Conversely, a positive phase shift will suggest the presence of a downwardly propagating wave, with a potential explanation incorporating aspects of wave reflection. However, the discrepancy between the amount of reflected waves in the observational (∼28% with positive phase angles) and simulated (∼5% with positive phase angles) time series may be related to the upper boundary conditions applied to the numerical simulations, in addition to noise aspects discussed above. The simulated upper boundary is at least partially reflective, but rigidly corresponds to a constant height in the photosphere. Contrarily, in the real Sun, this reflective layer can vary as a function of time and spatial position, potentially leading to a broader scatter of phase differences for the reflected wave.

3.2.2. Oscillation Frequency as a Function of Spatial Size

While it is clear from Figure 4 that a spread of oscillation frequencies is present in the data, it is important to investigate how individual photospheric structures affect the detected frequency. Following the procedures detailed in Krijger et al. (2001), power spectra for the *G*-band and 4170 Å continuum observations and

simulations are shown as a function of oscillation frequency and spatial wavenumber in the upper panels of Figures 7 and 8, respectively. In each spectra, the majority of oscillatory power is associated with low frequencies and large spatial scales, consistent with solar *p*-mode oscillations (Duvall et al. 1988). These lower-left portions of the observational and simulated spectra reveal power approaching six and ten orders of magnitude above the quiescent background, respectively, highlighting the considerable power associated with these waves. Moving to smaller spatial scales (i.e., higher wavenumbers), it is clear that higher oscillation frequencies tend to be associated with these structures. This effect is particularly pronounced in the upper panels of Figure 7, where a diagonal band of high oscillatory power is seen to stretch diagonally away from the lower-left corner of the power spectra. This can be verified in Figure 4, where oscillations down to ≈110 s can be detected in small-scale MBP structures, compared to a ≈160 s lower limit on typically larger, non-MBP regions.

It is interesting to note that almost no oscillations with periodicities below 100 s are detected simultaneously in the *G*-band and 4170 Å continuum data sets. This applies to both the observational and simulated data, but may be related to the
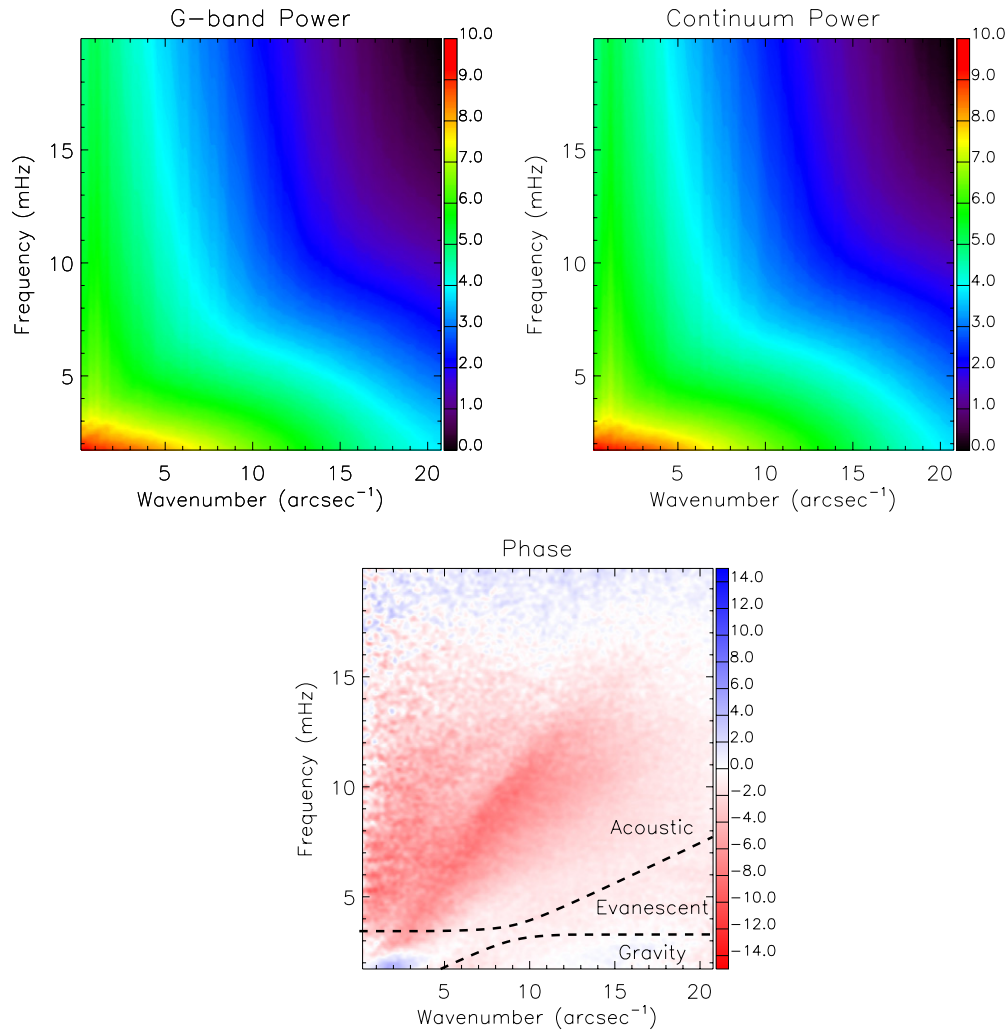
Figure 8. Power spectra of the *G*-band (upper left) and 4170 Å continuum (upper right) simulations as a function of frequency and spatial wavenumber. The color scale represents the power (in orders of magnitude) above the quiescent background. The lower panel shows the phase delay between the *G*-band and 4170 Å continuum oscillations as a function of frequency and spatial wavenumber. The color scale is in degrees, where positive and negative values indicate that the *G* band leads, and trails, the 4170 Å continuum, respectively. Limiting curves for acoustic- and gravity-wave regimes are displayed as dashed lines, with an evanescent region sandwiched between the acoustic and gravity regimes. A similar figure, only for the observational time series, is shown in Figure 7.

(A color version of this figure is available in the online journal.)

broad filter widths used. Recently, Kneer & Bello González (2011) detected upwardly propagating waves in the lower solar atmosphere with periodicities as short as 70 s. The authors utilized two-dimensional spectral imaging techniques to obtain a time series with an extremely narrow equivalent bandpass (≈18 mÅ). Contrarily, the contribution functions extracted from our numerical simulations extend over a range of atmospheric heights due to the broad nature of our *G*-band and 4170 Å continuum filters, potentially decreasing and/or smoothing wave signals with periods shorter than 100 s. This does not necessarily mean that waves with periodicities below 100 s do not occur individually in either the *G*-band or 4170 Å continuum data sets. However, it does indicate that if these waves exist, we do not detect their propagation between atmospheric layers since no coherent signals can be determined. The phase distribution displayed in the lower panel of Figure 7 reveals a shift of ≈−10° between *G*-band and 4170 Å continuum oscillations, apparent down to a spatial scale of ∼0″.4 (wavenumber 15 arcsec⁻¹). This spatial size is consistent with typical (roundish) MBP diameters and forms an upper wavenumber limit beyond which the phase distribution becomes dominated

by noise. These measurements are in agreement with the occurrence plots presented in Figure 4 and reiterate the presence of upward propagating wave phenomena.

Examination of the lower panel of Figure 7 reveals a frequency "fork" for wavenumbers below 4 arcsec⁻¹ (spatial size of approximately 1″.6). This "fork" constitutes a continual linear downward trend of upwardly propagating waves (negative phases) for oscillation frequencies as a function of spatial wavenumber, in addition to a visible plateau at frequencies ranging from 4 to 7 mHz, which includes the 3 minute (≈5.5 mHz) *p*-mode oscillation. A plateau suggests that the frequency of detected oscillations is no longer dependent on the increasing size of the spatial dimension, at least up to the ≈70″ limit imposed by our field of view. As a result, upwardly propagating 3 minute oscillations appear to be ubiquitous over granular (and larger) spatial scales. This agrees with the theoretical work of Erdélyi et al. (2007), who demonstrate how 3 minute oscillations are free to propagate upward from the solar surface as a consequence of their frequency residing above the acoustic cutoff value. A 3 minute periodicity overlaps with the solar *p*-mode spectrum, which has been shown by Moretti et al. (2001) to exist
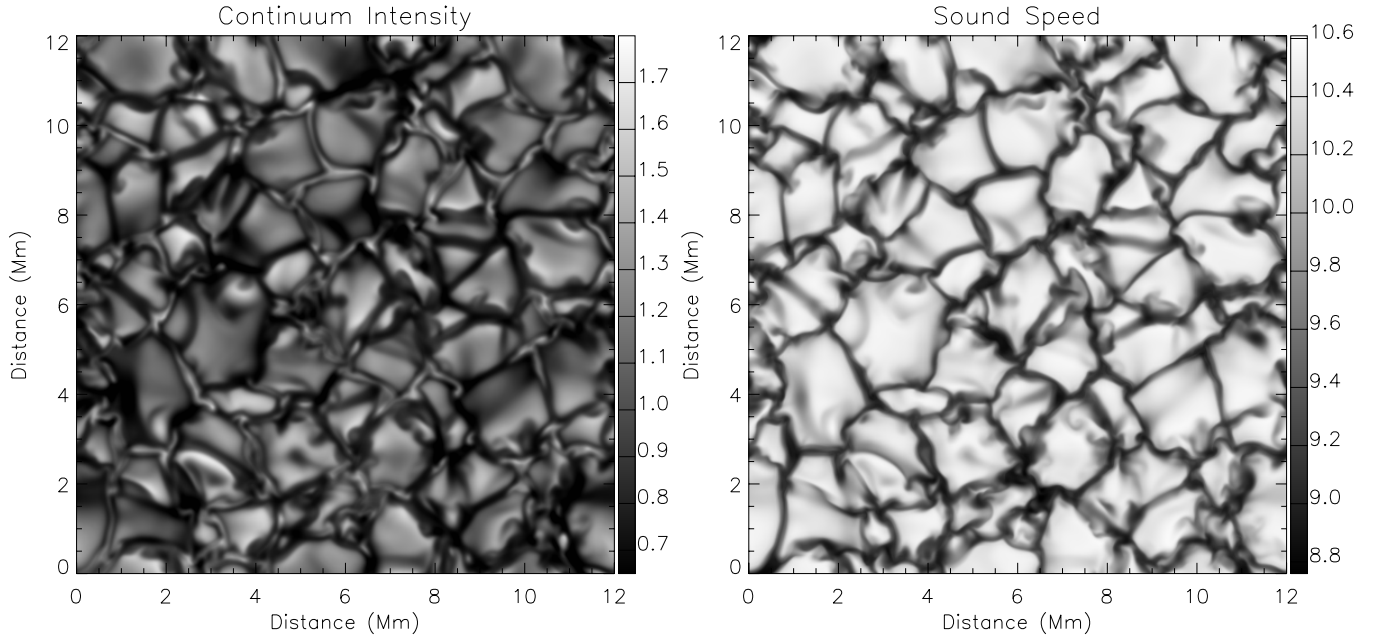
Figure 9. 4170 Å continuum intensity image (left), normalized to its mean, is displayed alongside the simultaneous pixelized sound speeds (right), where the color scale represents the derived sound speeds in km s^{-1}. The average sound speed for the entire simulated field of view is 10.1 km s^{-1}. All axes are distances along the solar surface, where 1 Mm = 1000 km $\simeq$ 1″.38.

as a result of coherent pressure drivers up to spatial scales consistent with supergranular cells ($\sim$50″). Thus, our results indicate an abundance of upwardly propagating longitudinal waves which cover the majority of our field of view and suggests these wave forms are a direct result of a coherent (supergranular) p-mode driver. Interestingly, a similar phase plateau is not apparent in the simulated frequency–wavenumber diagram (lower panel of Figure 8). This may be a direct result of the reduced field of view of the simulated time series. With an overall size of 16.5×16.5 arcsec^2, compared to the observational field of view of 69.3×69.1 arcsec^2, information occurring on large spatial scales (i.e., low wavenumbers) will be lost.

Evanescent waves are a phenomenon known to exist in the frequency–wavenumber diagram in locations of very low frequency and small wavenumber (Frazier 1968; Deubner 1975a; Lites & Chipman 1979; Deubner et al. 1990). These waves cover the global 5 minute oscillation ($\sim$3 mHz) and are not expected to show signals of upward propagation. Positioned on either side of the evanescent region are locations in the frequency–wavenumber diagram where acoustic and gravity waves thrive (Souffrin 1966; Stix 1970; Deubner 1975). To investigate which regime best matches our detected wave phenomena, theoretical curves incorporating acoustic-, evanescent-, and gravity-wave regimes, were overplotted in the phase diagrams of Figures 7 and 8. In order to do this, the pressure, P, and density, ρ, were first extracted from our numerical simulations. Then, the sound speed, c_s, can be determined for each grid cell in our numerical domain using,

$$c_s = \sqrt{\frac{\gamma P}{\rho}}, \qquad (4)$$

where γ is the ratio of specific heats, here taken as 5/3. The pixelized sound speeds were then convolved with our bandpass-specific contribution functions to determine an accurate representation of the sound speeds typically contained within our filtergrams. A two-dimensional representation of the derived sound speeds is shown in the right panel of Figure 9, with an

spatial average of 10.1 km s^{-1}. Using this value for the sound speed, and following the steps outlined in Kneer & Bello González (2011), we derived the limiting curves for acoustic- and gravity-wave regimes. These frequency–wavenumber contours are overplotted in the phase diagrams of Figures 7 and 8, with the locations of acoustic-, evanescent-, and gravity-wave regimes annotated. Close inspection of the lower panel in Figure 7 reveals how there are no upwardly propagating waves (i.e., negative phase angles) in areas of the diagram with frequencies less than $\sim$3 mHz (5 minutes) and wavenumbers less than $\sim$4 arcsec^{-1} (1″.6), consistent with previous studies of evanescent waves. In this portion of the frequency–wavenumber diagram, only downwardly propagating waves appear to prevail. A similar trend is detected in the simulated time series (lower panel of Figure 8), where downwardly propagating waves dominate for wavenumbers less than $\sim$4 arcsec^{-1} and frequencies less than $\sim$2.5 mHz. Slight differences between the observational and simulated frequency–wavenumber diagrams at these extreme limits of frequency and wavenumber may again be a result of the reduced field-of-view size and time-series length for the simulated data. Nevertheless, the observational and simulated phase distributions (lower panels of Figures 7 and 8) reveal identical trends, whereby propagating waves, best described as acoustic phenomena, with a similar phase angle increase in frequency with decreasing spatial size.

3.2.3. Wave Propagation Velocity

A phase difference of $-8°$ (as found in our observational time series), in conjunction with the most commonly occurring periodicity of 390 s, results in a time lag of 8.7 s between 4170 Å continuum and G-band atmospheric heights. Utilizing a traversed distance of 55–83 km, estimated through a comparison of G-band and 4170 Å continuum MBP contribution functions in our radiative MHD simulations, an average propagation speed of 7.9 ± 1.6 km s^{-1} is found. This derived wave speed is close to typical photospheric sound speeds, and reveals how, at least in the photospheric regime, the detected oscillations are linear in nature.

4. CONCLUDING REMARKS

Here, we present high-cadence observations and simulations of the solar photosphere. Each data set demonstrates a wealth of oscillatory behavior, with high concentrations found in highly magnetic regions, such as MBPs, visible as periodic intensity fluctuations with periods in the range 110–600 s. Using a high-resolution radiative MHD code to simulate photospheric magnetoconvection, we detect a wealth of upwardly propagating acoustic waves over a range of frequencies and wavenumbers. Results of the MHD simulations are consistent with those found in our observational time series, confirming that current MHD simulations are able to accurately replicate propagating wave phenomena in the lower solar atmosphere, without the need of an external driver. We suggest how the ubiquity of these oscillations may be traced back to magnetoconvective processes occurring in the upper layers of the Sun's convection zone. We are able to estimate the average height of formation of our G-band and 4170 Å continuum filters by convolving the filter bandpasses with the radiative output of our simulation. This provides minimum G-band and 4170 Å continuum formation heights of 100 km and 25 km, respectively. We find that longitudinal oscillations exhibit a dominant phase delay of $-8°$ between G-band and 4170 Å continuum observations, suggesting the presence of upwardly propagating waves. Almost no propagating waves with periods less than 100 s are detected in either observational or simulated data. This does not necessarily mean that these high-frequency oscillations do not occur individually in either bandpass. However, it does indicate that if these waves exist, we do not detect their propagation between atmospheric layers since no coherent signals can be determined. More than 73% of MBPs (73% from observations and 96% from simulations) display upwardly propagating wave phenomena, helping to explain the ubiquitous nature of MHD waves in the outer solar atmosphere.

REFERENCES

Afram, N., Unruh, Y. C., Solanki, S. K., et al. 2011, A&A, 526, A120
Beck, C., Schmidt, W., Rezaei, R., & Rammacher, W. 2008, A&A, 479, 213
Bello González, N., Flores Soriano , M., Kneer, F., & Okunev, O. 2009, A&A, 508, 941
Bello González, N., Flores Soriano , M., Kneer, F., Okunev, O., & Shchukina, N. 2010a, A&A, 522, A31
Bello González, N., Franz, M., Martínez Pillet, V., et al. 2010b, ApJ, 723, L134
Bogdan, T. J., Carlsson, M., Hansteen, V. H., et al. 2003, ApJ, 599, 626
Cally, P. S., & Goossens, M. 2008, Sol. Phys., 251, 251
Carlsson, M., Hansteen, V. H., de Pontieu, B., et al. 2007, PASJ, 59, 663
Carlsson, M., & Stein, R. F. 1997, ApJ, 481, 500
Cauzzi, G., Reardon, K., Rutten, R. J., Tritschler, A., & Uitenbroek, H. 2009, A&A, 503, 577
Crockett, P. J., Jess, D. B., Mathioudakis, M., & Keenan, F. P. 2009, MNRAS, 397, 1852
Crockett, P. J., Mathioudakis, M., Jess, D. B., et al. 2010, ApJ, 722, L188
DeForest, C. E. 2004, ApJ, 617, L89
De Pontieu, B., McIntosh, S., Hansteen, V. H., et al. 2007, PASJ, 59, 655
Deubner, F.-L. 1975a, A&A, 44, 371
Deubner, F.-L. 1975b, Sol. Phys., 40, 333
Deubner, F.-L., Fleck, B., Marmolino, C., & Severino, G. 1990, A&A, 236, 509
Duvall, T. L., Jr., Harvey, J. W., Libbrecht, K. G., Popp, B. D., & Pomerantz, M. A. 1988, ApJ, 324, 1158
Edwin, P. M., & Roberts, B. 1983, Sol. Phys., 88, 179
Erdélyi, R., Malins, C., Tóth, G., & de Pontieu, B. 2007, A&A, 467, 1299
Fedun, V., Shelyag, S., & Erdélyi, R. 2011a, ApJ, 727, 17
Fedun, V., Shelyag, S., Verth, G., Mathioudakis, M., & Erdélyi, R. 2011b, Ann. Geophys., 29, 1029
Fossum, A., & Carlsson, M. 2005, Nature, 435, 919
Frazier, E. N. 1968, Z. Geophys., 68, 345
Goode, P. R., Strous, L. H., Rimmele, T. R., & Stebbins, R. T. 1998, ApJ, 495, L27
Gurtovenko, E., Ratnikova, V., & de Jager, C. 1974, Sol. Phys., 37, 43
Hasan, S. S., & van Ballegooijen, A. A. 2008, ApJ, 680, 1542
Hoekzema, N. M., Rimmele, T. R., & Rutten, R. J. 2002, A&A, 390, 681
Jess, D. B., Andić, A., Mathioudakis, M., Bloomfield, D. S., & Keenan, F. P. 2007a, A&A, 473, 943
Jess, D. B., Mathioudakis, M., Christian, D. J., Crockett, P. J., & Keenan, F. P. 2010a, ApJ, 719, L134
Jess, D. B., Mathioudakis, M., Christian, D. J., et al. 2010b, Sol. Phys., 261, 363
Jess, D. B., Mathioudakis, M., Crockett, P. J., & Keenan, F. P. 2008, ApJ, 688, L119
Jess, D. B., Mathioudakis, M., Erdélyi, R., et al. 2009, Science, 323, 1582
Jess, D. B., McAteer, R. T. J., Mathioudakis, M., et al. 2007b, A&A, 476, 971
Kalkofen, W. 2007, ApJ, 671, 2154
Keys, P. H., Mathioudakis, M., Jess, D. B., et al. 2011, ApJ, 740, L40
Kitiashvili, I. N., Kosovichev, A. G., Mansour, N. N., & Wray, A. A. 2011, ApJ, 727, L50
Kneer, F., & Bello González, N. 2011, A&A, 532, A111
Krijger, J. M., Rutten, R. J., Lites, B. W., et al. 2001, A&A, 379, 1052
Kurucz, R. L. 1993, CDROM
Leighton, R. B. 1960, in IAU Symp. 12, Aerodynamic Phenomena in Stellar Atmospheres, ed. R. N. Thomas (Cambridge: Cambridge Univ. Press), 321
Lites, B. W., & Chipman, E. G. 1979, ApJ, 231, 570
Magain, P. 1986, A&A, 163, 135
Moretti, P. F., Cacciani, A., Hanslmeier, A., et al. 2001, A&A, 372, 1038
Morton, R. J., Erdélyi, R., Jess, D. B., & Mathioudakis, M. 2011, ApJ, 729, L18
Rees, D. E., Durrant, C. J., & Murphy, G. A. 1989, ApJ, 339, 1093
Rimmele, T. R. 2004, Proc. SPIE, 5490, 34
Rimmele, T. R., Goode, P. R., Harold, E., & Stebbins, R. T. 1995, ApJ, 444, L119
Rose, A. 1948, J. Opt. Soc. Am. (1917–1983), 38, 196
Sánchez Almeida, J., Bonet, J. A., Viticchié, B., & Del Moro, D. 2010, ApJ, 715, L26
Schroeder, D. J. (ed.) 2000, Astronomical Optics (San Diego, CA: Academic)
Schüssler, M., Shelyag, S., Berdyugina, S., Vögler, A., & Solanki, S. K. 2003, ApJ, 597, L173
Shelyag, S., Fedun, V., Keenan, F. P., Erdélyi, R., & Mathioudakis, M. 2011a, Ann. Geophys., 29, 883
Shelyag, S., Keys, P., Mathioudakis, M., & Keenan, F. P. 2011b, A&A, 526, A5
Shelyag, S., Mathioudakis, M., Keenan, F. P., & Jess, D. B. 2010, A&A, 515, A107
Shelyag, S., Mathioudakis, M., Keenan, F. P., et al. 2011c, A&A, submitted
Shelyag, S., Schüssler, M., Solanki, S. K., Berdyugina, S. V., & Vögler, A. 2004, A&A, 427, 335
Skartlien, R., Stein, R. F., & Nordlund, Å. 2000, ApJ, 541, 468
Souffrin, P. 1966, Ann. d'Astrophys., 29, 55
Spruit, H. C. 1976, Sol. Phys., 50, 269
Stein, R. F., & Leibacher, J. 1974, ARA&A, 12, 407
Stein, R. F., & Nordlund, Å. 1991, in Proc. Institute for Theoretical Physics, Challenges to Theories of the Structure of Moderate-Mass Stars, Vol. 388, ed. D. Gough & J. Toomre (Berlin: Springer), 195
Stix, M. 1970, A&A, 4, 189
Straus, T., Fleck, B., Jefferies, S. M., et al. 2008, ApJ, 681, L125
Taroyan, Y., & Erdélyi, R. 2009, Space Sci. Rev., 149, 229
Torrence, C., & Compo, G. P. 1998, Bull. Am. Meteorol. Soc., 79, 61
Vecchio, A., Cauzzi, G., Reardon, K. P., Janssen, K., & Rimmele, T. 2007, A&A, 461, L1
Vögler, A., Shelyag, S., Schüssler, M., et al. 2005, A&A, 429, 335
Wedemeyer, S., Freytag, B., Steffen, M., Ludwig, H.-G., & Holweger, H. 2003, Astron. Nachr., 324, 410
Wedemeyer, S., Freytag, B., Steffen, M., Ludwig, H.-G., & Holweger, H. 2004, A&A, 414, 1121
Wöger, F., von der Lühe, O., & Reardon, K. 2008, A&A, 488, 375